

Possible metamagnetism in the high-pressure tetragonal phase of  $\text{UTe}_2$ T. Thebault <sup>1</sup>, D. Braithwaite <sup>2</sup>, G. Lapertot,<sup>2</sup> D. Aoki <sup>3</sup>, G. Knebel <sup>2</sup> and W. Knafo <sup>1</sup><sup>1</sup>Laboratoire National des Champs Magnétiques Intenses - EMFL, CNRS, Université Grenoble Alpes, INSA-T, Université Toulouse 3, 31400 Toulouse, France<sup>2</sup>Université Grenoble Alpes, CEA, Grenoble INP, IRIG, PHELIQS, 38000, Grenoble, France<sup>3</sup>Institute for Materials Research, Tohoku University, Ibaraki 311-1313, Japan

(Received 29 March 2024; revised 16 May 2024; accepted 20 May 2024; published 13 June 2024)

A structural orthorhombic-to-tetragonal phase transition was recently discovered in the heavy-fermion compound  $\text{UTe}_2$  at a pressure  $p^* \simeq 3 - 8$  GPa [Honda *et al.*, *J. Phys. Soc. Jpn.* **92**, 044702 (2023); Huston *et al.*, *Phys. Rev. Mater.* **6**, 114801 (2022)]. In the high-pressure tetragonal phase, a phase transition at  $T_x = 235$  K and a superconducting transition at  $T_{sc} = 2$  K have been revealed. In this work we present an electrical-resistivity study of  $\text{UTe}_2$  in pulsed magnetic fields up to  $\mu_0 H = 58$  T combined with pressures up to  $p = 6$  GPa. The field was applied in a direction tilted by  $30^\circ$  from  $\mathbf{b}$  to  $\mathbf{c}$  in the orthogonal structure, which is identified as the direction  $\mathbf{c}'$  of the tetragonal structure. In the tetragonal phase, the presence of superconductivity is confirmed and signatures of metamagnetic transitions are observed at the fields  $\mu_0 H_{x1} = 24$  T and  $\mu_0 H_{x2} = 34$  T and temperatures smaller than  $T_x$ . We discuss the effects of uniaxial pressure, and we propose that a magnetic ordering drives the transition at  $T_x$ .

DOI: [10.1103/PhysRevB.109.214420](https://doi.org/10.1103/PhysRevB.109.214420)

## I. INTRODUCTION

$\text{UTe}_2$  was extensively studied in the past few years [1,2]. It is orthorhombic and has anisotropic electrical and magnetic properties at ambient pressure [3–6]. This heavy-fermion paramagnet [7] is superconducting below  $T_{sc} = 1.5 - 2.1$  K at ambient pressure (phase SC1) and was presented as a candidate for triplet superconductivity [6,8]. A reinforcement of superconductivity under a magnetic field  $\mu_0 H > 15$  T applied along direction  $\mathbf{b}$  [9,10], arises from the stabilization of a high-magnetic-field superconducting phase (SC2) [11]. The presence of a second reentrant superconducting phase (SC-PPM), which is fully decoupled from SC1, was found for a magnetic field tilted by  $30^\circ$  from  $\mathbf{b}$  toward  $\mathbf{c}$  [10,12–15]. The two superconducting phases SC2 and SC-PPM are closely related to a metamagnetic transition at the field  $H_m$  [16,4]. By considering the three dimensions of field directions, the domain of stability of SC-PPM was further identified as a distorted halo [17,18]. At ambient pressure and zero field, quasi-two-dimensional antiferromagnetic (AF) fluctuations have been detected [19–23]. They are gapped in the superconducting phase SC1 [24,25] and are probably involved in the superconducting pairing mechanism [26]. The Fermi-liquid electrical-resistivity coefficient  $A$  and NMR relaxation rates are peaked at  $H_m$ , indicating the presence of critical magnetic fluctuations which may play a role for the field-induced superconducting phases [12,16,27,28]. Theoretical works considered the relation between superconductivity and the magnetic fluctuations [29–32] and symmetries of the different superconducting phases [33,34].

Under pressure  $p$ , SC1 is suppressed with a linear decrease with  $p$  of the associated critical temperature, and a second superconducting phase SC2 appears at pressures larger than 0.3 GPa, with a maximal critical temperature  $T_{sc} \simeq 3$  K

at  $p \simeq 1.2$  GPa [35–39]. Similar saturations of the NMR Knight shifts below  $T_{sc}$  [38] and a boundary between SC1 and SC2 in the low-temperature ( $p, H$ ) phase diagram by tunnel-diode-oscillator technique [40] have been determined. They suggest that the superconducting phase stabilized under pressure may be the same phase SC2 as that induced by a magnetic field, which needs now to be confirmed by thermodynamic measurements, such as heat capacity or thermal expansion, under pressure combined with magnetic field. Magnetic-susceptibility measurements showed a change of the magnetic anisotropy at the critical pressure  $p_c \simeq 1.7$  GPa [38,41–43], beyond which superconductivity disappears and an incommensurate antiferromagnetic order is established [35,44]. Pressure was also combined with magnetic fields in different directions, unveiling additional field-induced superconducting phases [36,40,45–51].

Recently, a study by electrical-resistivity measurements combined with single-crystal x-ray diffraction under pressures up to  $p = 10$  GPa showed the presence of a structural transition at  $p^* \simeq 3 - 8$  GPa from a low-pressure orthorhombic structure with the space group  $Immm$  into a high-pressure tetragonal structure with the space group  $I4/mmm$  [52] (see Fig. 1). The structural transition was confirmed by powder x-ray diffraction studies under pressure up to  $p = 24$  GPa [53] and 30 GPa [54] and related with a valence change [54,55]. A structural transition was also predicted in [56]. In the tetragonal phase, a kink in the electrical resistivity indicates a phase transition at temperature  $T_x \simeq 235$  K [46,47,52], and a superconducting phase develops below  $T_{sc} = 2$  K [52]. A transition under a magnetic field was also seen in  $\text{UTe}_2$  in its high-pressure tetragonal phase at temperatures below  $T_x$ , and its trace at around 30 T was lost at low temperature [46,47]. However, in that study the uncertainty in the magnetic-field direction  $\mathbf{H} \simeq \|\mathbf{b}$  was large, with an estimated misorientation

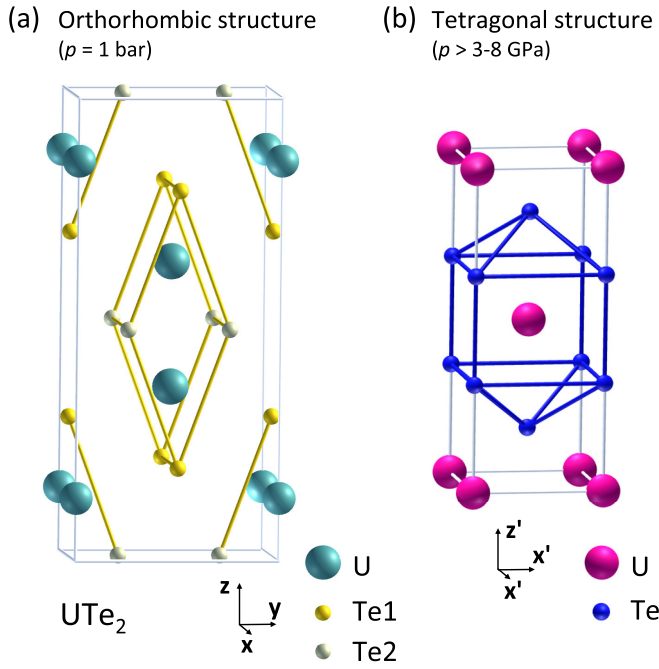


FIG. 1. Unit cells of  $\text{UTe}_2$  (a) in its low-pressure orthorhombic structure and (b) in its high-pressure tetragonal structure.

of  $\simeq 15^\circ - 30^\circ$ , due to a sample positioning issue in the pressure cell (see discussion in the Supplemental Material [57]).

Here we present electrical-resistivity measurements performed on a  $\text{UTe}_2$  single crystal under pressure up to  $p = 6$  GPa and magnetic field up to  $\mu_0 H \simeq 58$  T. The magnetic field was applied along a direction tilted by  $30^\circ$  from  $\mathbf{b}$  toward  $\mathbf{c}$  in the orthorhombic structure. Signatures of the tetragonal phase are found for  $p \geq 3.1$  GPa. Magnetic-field-temperature phase diagrams are constructed for the different pressures. The Fermi-liquid coefficient  $A$  is extracted from measurements made in the orthorhombic phase. In the tetragonal phase, we confirm the presence of superconductivity, and transitions with a large hysteresis at  $\mu_0 H_{x1} = 24$  T and  $\mu_0 H_{x2} = 34$  T are identified as possible metamagnetic transitions.

## II. METHODS

The  $\text{UTe}_2$  single crystal measured here was grown by the molten-salt-flux method [58]. Its electrical resistivity  $\rho_{xx}$  was measured with an electrical current along  $\mathbf{a}$  under magnetic fields  $\mu_0 \mathbf{H}$  up to 58 T tilted by  $30^\circ$  from  $\mathbf{b}$  toward  $\mathbf{c}$ . The field was combined with pressures up to 6 GPa and temperatures down to 1.4 K. The sample was polished with a tilt by an angle of  $7^\circ$  from a cleaving surface normal to the direction  $\mathbf{n}$  of Miller indices (0,1,1) (see [20]), ending in two faces normal to a direction tilted by  $30^\circ$  from  $\mathbf{b}$  towards  $\mathbf{c}$ . The orientation of the crystal was ensured by Laue diffraction after the polishing process. Its electrical resistivity was measured using the four-contact technique, with an excitation current of 4 mA at a frequency of  $\simeq 50$  KHz. Pulsed-magnetic-field experiments were performed using long-duration 60-T magnets at the LNCMI-Toulouse. Here we used a Bridgman-type cell specifically designed for the pulsed magnetic fields [59]. To avoid substantial heating by eddy currents, ceramic anvils

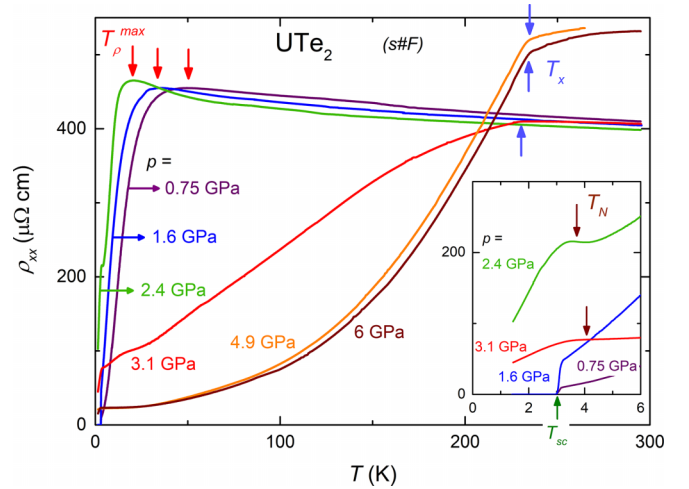


FIG. 2. Temperature dependence of the electrical resistivity  $\rho_{xx}$ , measured with  $\mathbf{I} \parallel \mathbf{a}$ , of  $\text{UTe}_2$  under different hydrostatic pressures and zero magnetic field. Inset: Zoom on the onset of superconductivity and antiferromagnetic order at low temperature.

and a pyrophyllite gasket were used in the cell, whose body is made of MP35N. Most of the data presented here correspond to the rise of the field pulses, where the heating of the sample due to eddy currents in the cell is estimated, for 58-T pulses, to be less than 0.1 K at temperatures  $T \leq 4.2$  K, close to 1–1.5 K at temperatures from 5 K to 20 K and negligible at higher temperatures. For the falling-field data considered in this manuscript, the heating effects were evaluated during the pulse and are detailed in the Supplemental Material [57]. For low-field pulses ( $\mu_0 H \leq 30$  T), heating effects were negligible. Pressure was changed at room temperature and was estimated by measuring the superconducting transition temperature of a lead gauge. More information about the pressure cell setup can be found in two technical papers [59,60].

## III. RESULTS

### A. Overview

Figure 2 compares the temperature dependence of the electrical resistivity  $\rho_{xx}$  for different pressures  $p$  from 0.75 to 6 GPa. At  $p = 0.75$  and 1.6 GPa, superconductivity develops below  $T_{sc} \simeq 3$  K. The characteristic temperature  $T_\rho^{\max}$  of the maximum in resistivity is decreasing with increasing pressure from  $p = 0.75$  GPa to 2.4 GPa. We see the onset of the antiferromagnetic order at the Néel temperature  $T_N = 3.7$  K for the pressures  $p = 2.4$  GPa and  $p = 3.1$  GPa, i.e., above the critical pressure  $p_c \simeq 1.7$  GPa. This AF order is identified as a signature of the orthorhombic phase [44]. A kink at  $T_x \simeq 235$  K is visible in the electrical resistivity measured for  $p \geq 3.1$  GPa. Such a kink was also observed in the tetragonal phase in [52] and, in the following, we will identify it as a signature of the tetragonal phase. At  $p = 3.1$  GPa, signatures of both  $T_N$  and  $T_x$  indicate the coexistence of domains with the orthorhombic and tetragonal phases. At  $p = 4.9$  GPa and 6 GPa, the onset of superconductivity in the tetragonal phase is identified at  $\simeq 3$  K, and the electrical resistivity increases monotonously with temperature up to  $T_x$ . At  $p = 6$  GPa,

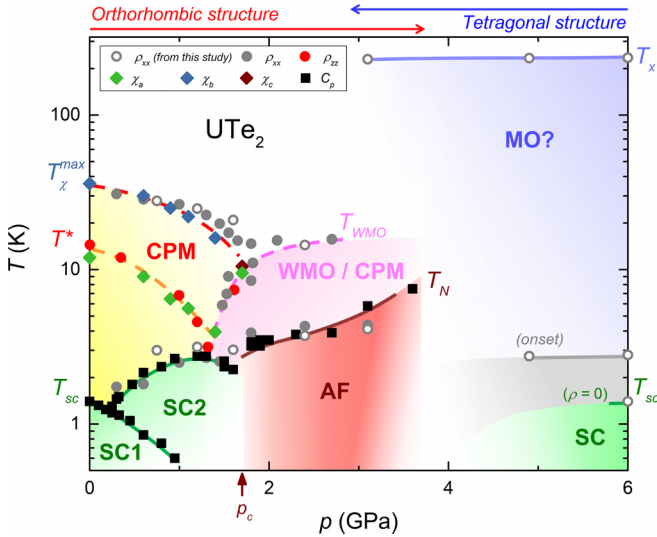


FIG. 3. Pressure-temperature phase diagram of  $\text{UTe}_2$  obtained from data published in Refs. [35] (heat capacity  $C_p$ ), [41] (magnetic susceptibilities  $\chi_a$ ,  $\chi_b$ , and  $\chi_c$ ), [46] (electrical resistivity  $\rho_{xx}$ ), [51] (electrical resistivity  $\rho_{zz}$ ), and data collected here (electrical resistivity  $\rho_{xx}$ ). CPM denotes the correlated paramagnetic regime, WMO/CPM the weak magnetic order/correlated paramagnetic regime, SC1, SC2, and SC the different superconducting phases, AF the antiferromagnetic phase, and MO? a suspected magnetically ordered phase.

superconductivity with zero resistivity is observed at temperatures below  $T_{sc} = 1.45$  K.

Figure 3 presents the pressure-temperature phase diagram obtained from data collected here and data published in [35,41,46,51]. The low-pressure region exhibits two crossovers at  $T_\chi^{\max} \simeq 35$  K and  $T^* \simeq 15$  K, and two different superconducting phases SC1 and SC2. The first crossover at  $T_\chi^{\max}$  is associated with a maximum in the magnetic susceptibility measured in a magnetic field along  $\mathbf{b}$  [3,4,41] and with a maximum in  $\Delta\rho_{xx}$  obtained after a background subtraction to the electrical resistivity  $\rho_{xx}$  [46]. It delimits a correlated paramagnetic (CPM) regime. The second crossover at  $T^* \simeq 15$  K is associated with a kink in the magnetic susceptibility measured in a magnetic field along  $\mathbf{a}$  and a maximum in the electrical resistivity  $\Delta\rho_{zz}$  (here subtracting a background has little effect due to the smaller temperature scale) [28,51]. The stabilization of quasi-two-dimensional antiferromagnetic fluctuations is suspected to drive the anomalies observed in bulk quantities at the characteristic temperature  $T^*$  [20,22,23]. The two crossover temperatures decrease with increasing pressure up to the critical pressure  $p_c \simeq 1.7$  GPa. Above this critical pressure, antiferromagnetic order is established below  $T_N \simeq 3.5$  K (defined here at the inflection point of  $\rho_{xx}$  versus  $T$ ), and a crossover is observed at  $T_{WMO} \simeq 8\text{--}12$  K in electrical-resistivity (defined at a kink near  $p_c$  or a maximum much beyond  $p_c$  of  $\rho_{xx}$  versus  $T$ ) [46,47,57] and magnetic-susceptibility data [41].  $T_{WMO}$  is the onset of a weak-magnetic-order regime, which is delimited by a maximum in the magnetic susceptibility and by a metamagnetic transition, and can be also identified as a CPM regime (see [46]). This regime is noted WMO/CPM here.

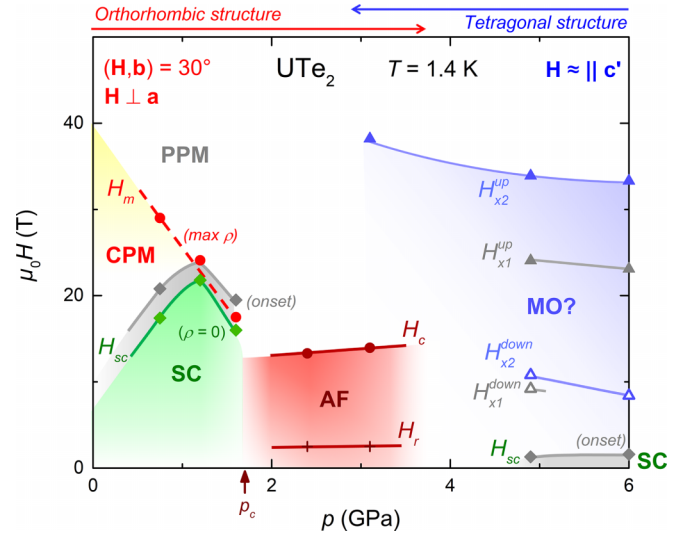


FIG. 4. Pressure-magnetic-field phase diagram of  $\text{UTe}_2$  at  $T = 1.4$  K and under a magnetic field tilted by  $30^\circ$  from  $\mathbf{b}$  toward  $\mathbf{c}$  (low-pressure orthorhombic structure) or along  $\simeq \mathbf{c}'$  (high-pressure tetragonal structure). CPM denotes the correlated paramagnetic regime, PPM the polarized paramagnetic regime, SC superconductivity, AF the antiferromagnetic phase, and MO? a suspected magnetically ordered phase.

At  $p = 3.1$  GPa, signatures of domains with the orthorhombic and tetragonal structures are observed in our data. By further increasing the pressure, the tetragonal phase is fully stabilized. The orthorhombic antiferromagnetic phase is no longer visible and the onset of the tetragonal superconducting phase is observed. Differences between the critical pressure  $p^* \lesssim 3$  GPa of the structural transition determined using the same pressure cells here and in [46] and the large set of critical pressures  $p^* \simeq 3\text{--}8$  GPa reported in [52,53] may be due to nonhydrostatic conditions of pressure (see discussion in Sec. IV C).

Figure 4 shows the pressure-magnetic-field phase diagram obtained here at  $T \simeq 1.4$  K. Details about the data are given in Secs. III B and III C. The magnetic field is tilted by  $30^\circ$  from  $\mathbf{b}$  toward  $\mathbf{c}$  in the orthorhombic phase. We will see in Sec. IV B that this field direction is identified as the direction  $\mathbf{c}'$  of the tetragonal phase. In the orthorhombic phase, superconductivity is enhanced under pressure and is delimited by the metamagnetic transition for  $1.1 \text{ GPa} \leq p \leq p_c$ . The boundaries between two superconducting phases (for instance, SC1 and SC2, which were identified from heat-capacity measurements in [35]) cannot be extracted from electrical-resistivity measurements, and superconductivity is simply noted SC in Figs. 4 and 5 determined here by electrical resistivity. The metamagnetic field  $H_m$  weakens when the pressure is increased, and no signature of  $H_m$  is found above the critical pressure  $p_c \simeq 1.7$  GPa. For  $p > p_c$ , an antiferromagnetic order is stabilized [44] and its phase is delimited by the critical field  $H_c$ . For  $p \geq 4.9$  GPa, no signature of the electronic properties in the orthorhombic structure is found, and two transitions at fields  $H_{x1}$  and  $H_{x2}$  are observed with a large hysteresis.  $H_{xi}^{\text{up}}$  and  $H_{xi}^{\text{down}}$  (for  $i = 1, 2$ ) respectively denote the transition field observed during the rise and fall of the

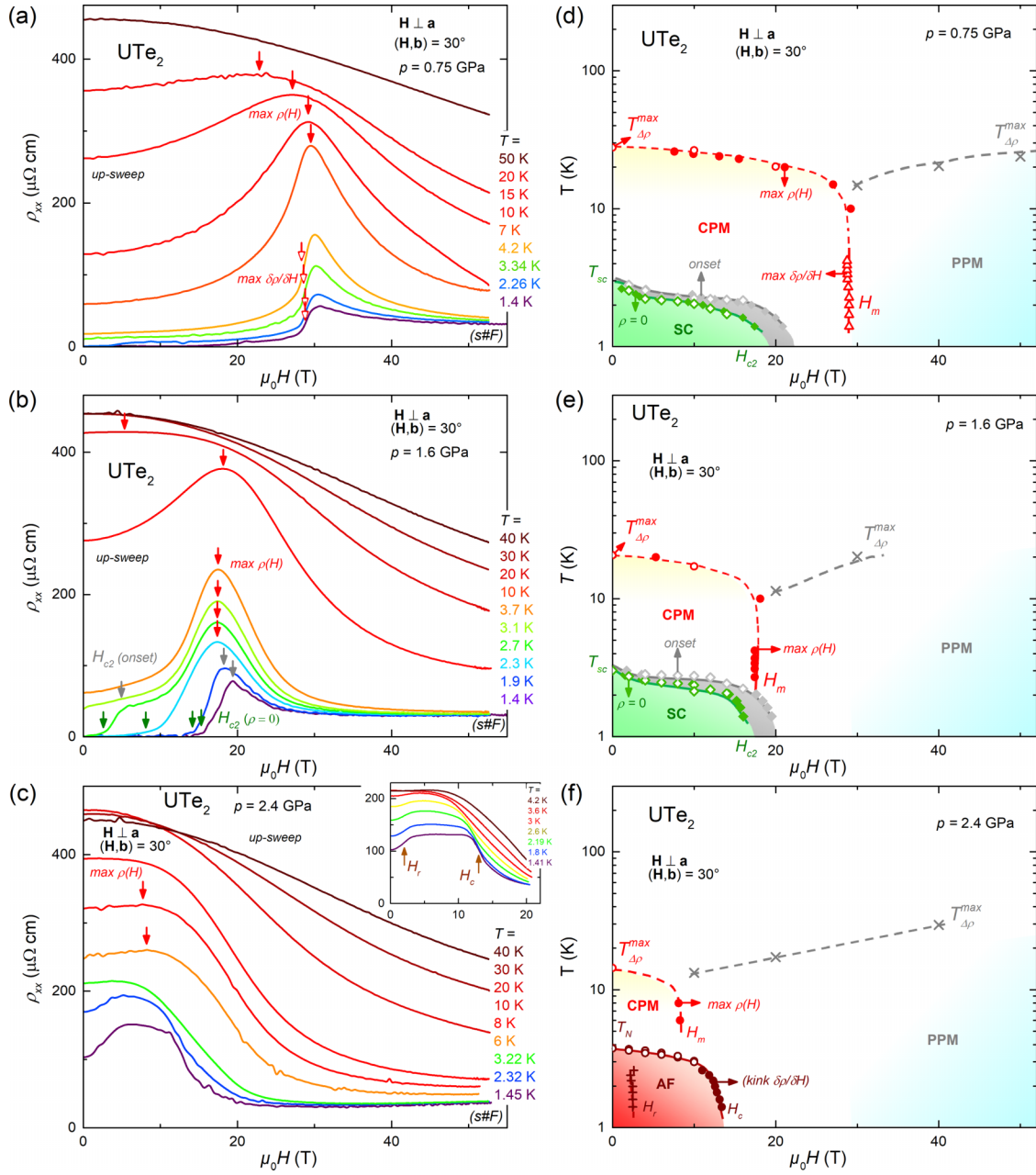


FIG. 5. Left-hand graphs: Electrical resistivity vs magnetic field at temperatures between 1.4 K and 50 K and pressures (a)  $p = 0.75$  GPa, (b)  $p = 1.6$  GPa, and (c)  $p = 2.4$  GPa. The data were obtained during the rise of the magnetic field. Right-hand graphs: Magnetic-field-temperature phase diagrams at (d)  $p = 0.75$  GPa, (e)  $p = 1.6$  GPa, and (f)  $p = 2.4$  GPa. CPM denotes the correlated paramagnetic regime, PPM denotes the polarized paramagnetic regime, SC superconductivity, and AF the antiferromagnetic phase. In [(d)–(f)], open symbols correspond to points extracted from  $\rho(T)$  data and closed symbols correspond to points extracted from  $\rho(H)$  data.

magnetic field. At  $p = 6$  GPa, the boundary of the superconducting phase is observed at  $\mu_0 H_{c2} \simeq 1.5$  T. At  $p = 3.1$  GPa, the transitions at  $\mu_0 H_c = 13.5$  T and  $\mu_0 H_{x2} = 38$  T are identified, implying a probable coexistence of orthorhombic and tetragonal domains.

### B. Orthorhombic phase

Figures 5(a)–5(c) present electrical-resistivity data obtained at pressures from  $p = 0.75$  GPa to 2.4 GPa for temperatures ranging from  $T = 1.4$  K to 50 K. Details about

the definition of the transition and crossover fields are given in the Supplemental Material [57]. At  $p = 0.75$  GPa and at low temperatures, a steplike transition in the resistivity is the signature of the metamagnetic transition at  $\mu_0 H_m = 29$  T. At higher temperatures this transition turns into a broad maximum. At  $p = 1.6$  GPa, the signature of the metamagnetic transition is masked by the onset of superconductivity at low temperature. At  $p = 2.4$  GPa, the antiferromagnetic order is stabilized below  $T_N = 3.7$  K. At temperatures  $T < T_N$ , kinks in the electrical resistivity are observed at the magnetic fields  $\mu_0 H_r$  and  $\mu_0 H_c$ , which reach 2.5 and 13.5 T, respectively, at

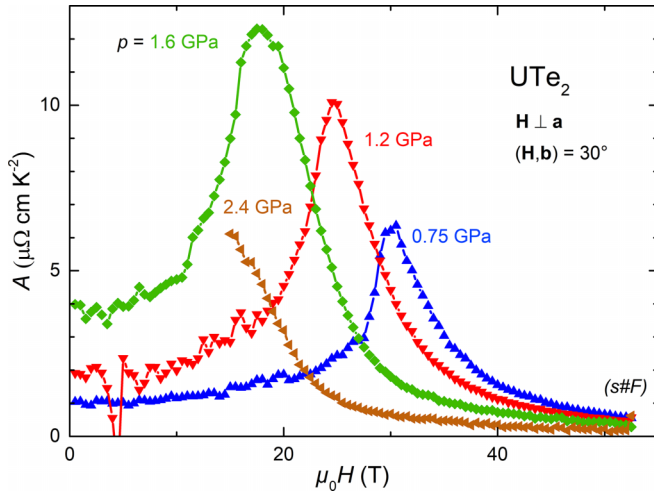


FIG. 6. Field dependence of the Fermi-liquid electrical-resistivity coefficient  $A$  of  $\text{UTe}_2$  at different pressures up to 2.4 GPa in a magnetic field tilted by  $30^\circ$  from  $\mathbf{b}$  toward  $\mathbf{c}$ .

low temperature (see also Ref. [46]). Figures 5(d)–5(f) show the magnetic-field-temperature phase diagrams obtained from our resistivity data at pressures  $p = 0.75$  GPa, 1.6 GPa, and 2.4 GPa, respectively. At  $p = 0.75$  GPa and 1.6 GPa,  $H_{c2}$  exhibits a change of curvature at  $T \simeq 2.4$  K, whose origin is not understood so far. The low-temperature superconducting field  $\mu_0 H_{c2}$  reaches  $\simeq 17$  T at  $p = 1.6$  GPa, i.e., near the critical pressure, here for  $\mathbf{H}$  tilted by  $30^\circ$  from  $\mathbf{b}$  towards  $\mathbf{c}$ , which is strongly enhanced in comparison with that of  $\simeq 6$  T found for  $\mathbf{H} \parallel \mathbf{b}$  [45]. The fields and temperatures, respectively defined at the broad maxima in  $\rho_{xx}(H)$  and  $\Delta\rho_{xx}(T)$ , which was obtained after a background subtraction as done in previous studies [28,46], delimit the CPM regime (see details in the Supplemental Material [57]). At  $p = 2.4$  GPa, the antiferromagnetic phase is delimited by  $H_c$  and no trace of superconductivity is found at low temperature.

Figure 6 shows the field dependence of the Fermi-liquid coefficient  $A$  determined under pressures up to  $p = 2.4$  GPa. The fits by  $\rho = \rho_0 + AT^2$  to the data used to extract  $A$  were performed at temperatures  $T_{sc} < T \leq 4.2$  K. Details about the fits are provided in the Supplemental Material [57]. At pressures  $p = 0.75$  GPa, 1.2 GPa, and 1.6 GPa, the coefficient  $A$  exhibits a maximum at  $H_m$ . At  $p = 2.4$  GPa, the electrical resistivity does not follow a quadratic temperature dependence in the antiferromagnetic phase for  $H < H_c$ . A decrease of  $A$  with an increasing magnetic field is observed in the polarized paramagnetic regime reached for  $H > H_c$ . For  $p \geq 3.1$  GPa, the electrical resistivity does not follow a  $T^2$  behavior at all fields investigated here.

### C. Tetragonal phase

Figure 7(a) shows the electrical resistivity measured at  $p = 4.9$  GPa and  $T = 1.45$  K for the rise and fall of pulsed magnetic fields of different strengths, from 20 T to 40 T. At  $p = 4.9$  GPa,  $\text{UTe}_2$  is in its tetragonal phase and the magnetic field is applied near to the direction  $\mathbf{c}'$  of the tetragonal structure (see Sec. IV B). A transition with a steplike variation of  $\rho$  by  $\simeq 2 \mu\Omega \text{ cm}$  occurs at  $\mu_0 H_{x1}^{\text{up}} = 24$  T during the rise of

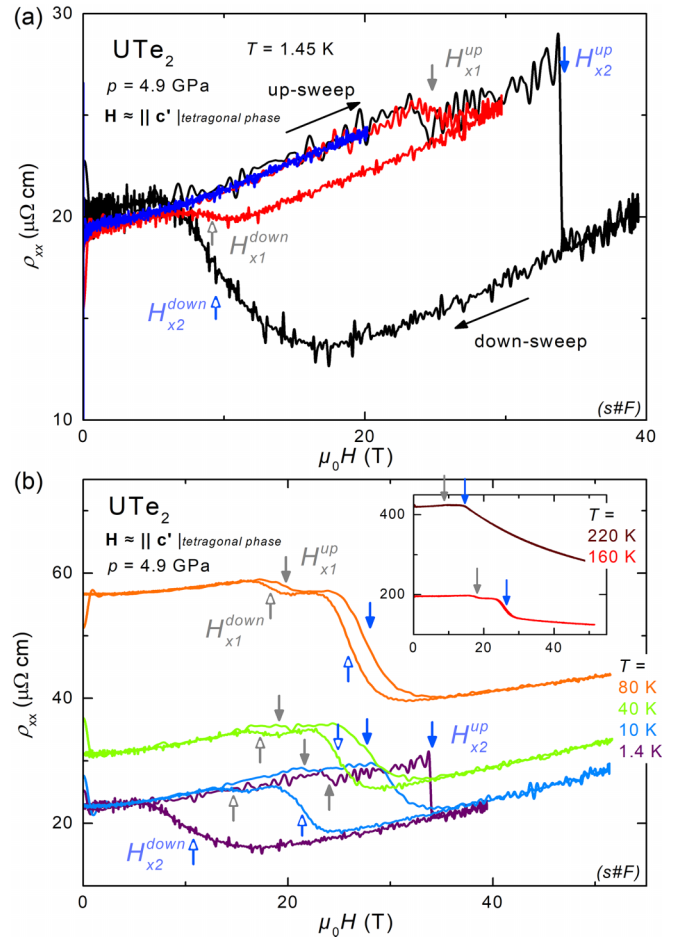


FIG. 7. (a) Magnetic-field dependence of the electrical resistivity  $\rho_{xx}$  of  $\text{UTe}_2$  at  $T = 1.4$  K and  $p = 4.9$  GPa obtained from pulsed-field shots of different strengths. (b) Magnetic-field dependence of the electrical resistivity  $\rho_{xx}$  of  $\text{UTe}_2$  at  $p = 4.9$  GPa and temperatures varying from 1.4 K to 220 K. Data obtained during the rise and fall of the pulse are shown here. Closed arrows indicate the transition fields in the rise of the field and open arrows indicate the transition fields in the fall of the field.

the magnetic field. This transition has a strong hysteresis and is characterized by the field  $\mu_0 H_{x1}^{\text{down}} = 9$  T during the fall of the magnetic field. A second transition with a larger steplike variation of  $\rho$ , by  $\simeq 10 \mu\Omega \text{ cm}$ , occurs at  $\mu_0 H_{x2}^{\text{up}} = 34$  T in the rising fields. This second transition has also a large hysteresis and is characterized by the field  $\mu_0 H_{x2}^{\text{down}} = 9.5$  T in the falling fields.  $H_{x2}^{\text{down}}$  and  $H_{x1}^{\text{down}}$  cannot be distinguished for the most intense magnetic-field pulses (up to more than 34 T). The initial state is recovered at the end of the magnetic-field pulse for  $H < H_{x1}^{\text{down}}$ . We note that due to eddy currents generated in the pressure cell, heating effects during the 42-T magnetic-field pulses lead to a temperature increase on the sample estimated by  $\Delta T = 0.1$  K at the maximum field and  $\Delta T = 0.6$  K at the end of the pulse, which has a small influence on the data presented here. Figure 7(b) presents the electrical resistivity for temperatures varying from 1.4 K to 220 K measured under a magnetic field up to 60 T at pressure  $p = 4.9$  GPa. By increasing the temperature, the signatures at the two transitions become broader; their hysteresis weakens

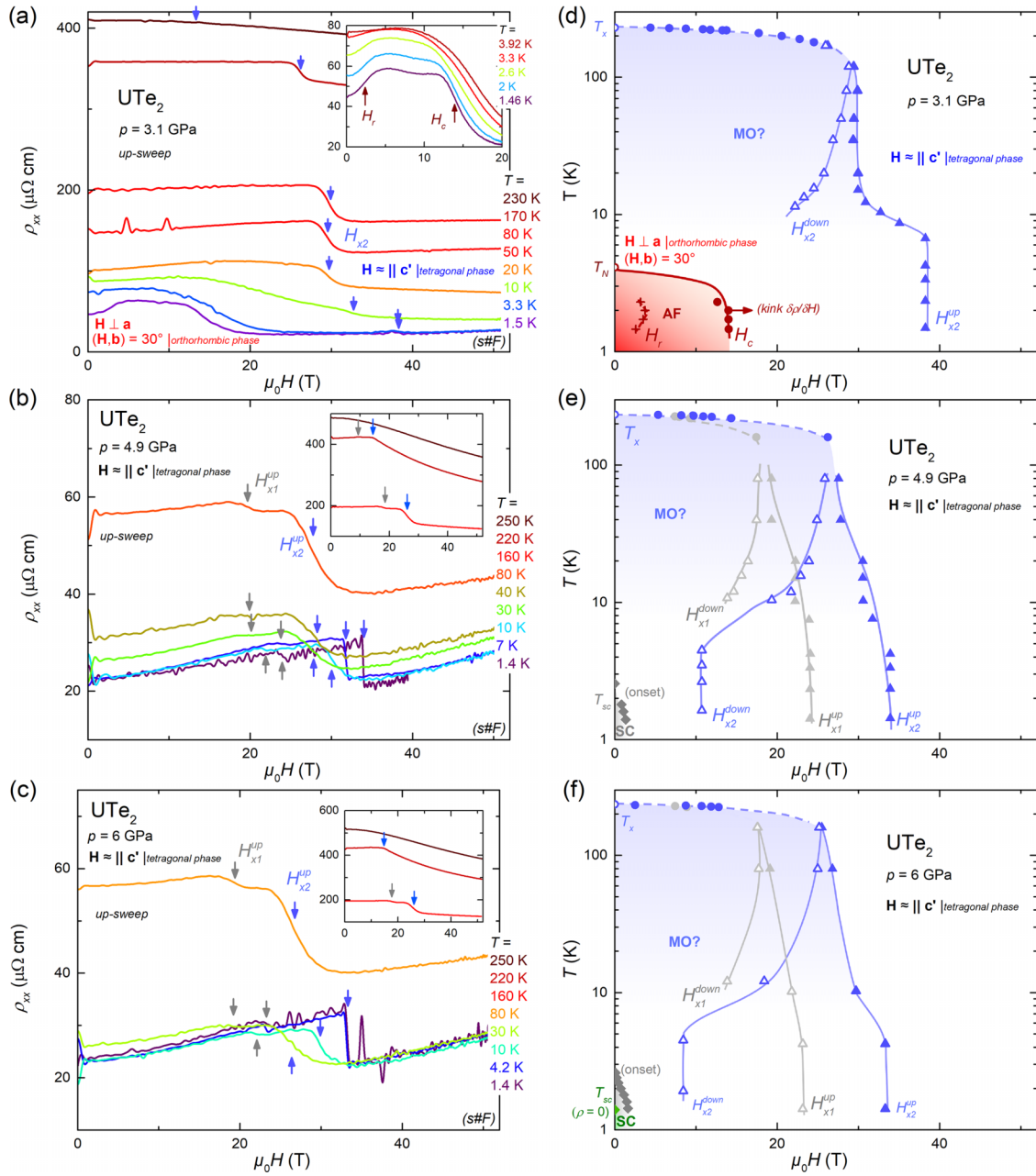


FIG. 8. Left-hand graphs: Electrical resistivity  $\rho_{xx}$  versus magnetic field  $H$  at temperatures between 1.4 K and 250 K and pressures (a)  $p = 3.1$  GPa, (b)  $p = 4.9$  GPa, and (c)  $p = 6$  GPa. The data were obtained during the rise of the magnetic field. Right-hand graphs: Magnetic-field-temperature phase diagrams at (d)  $p = 3.1$  GPa, (e)  $p = 4.9$  GPa, and (f)  $p = 6$  GPa. SC denotes superconductivity, AF the antiferromagnetic phase, and MO? a suspected magnetically ordered phase.

and disappears at temperatures higher than 160 K. At temperatures  $T \geq 10$  K, the characteristic fields  $H_{x1}^{\text{down}}$  and  $H_{x2}^{\text{down}}$  can be easily distinguished from each other.

Figures 8(a)–8(c) present the field dependence of the electrical resistivity measured at pressures  $p$  from 3.1 GPa to 6 GPa, from the rises of the field pulses. At  $p = 3.1$  GPa, the low-temperature electrical resistivity shows kinks at fields  $H_r$  and  $H_c$ , which are characteristic of the orthorhombic antiferromagnetic phase, and a step driven by a transition at the field  $H_{x2}$ , which is characteristic of the tetragonal phase. The anomaly at  $H_{x2}$  weakens at high temperature and only a kink is visible at  $T = 230$  K. At  $p = 4.9$  GPa and 6 GPa, two

transitions are observed at the fields  $H_{x1}$  and  $H_{x2}$ , at temperatures from  $T = 1.4$  K to 235 K, and no signature of the orthorhombic antiferromagnetic phase is found. No signatures of  $H_{x1}$  and  $H_{x2}$  are observed at temperatures larger than  $T_x = 235$  K. Figures 8(d)–8(f) present the magnetic-field-temperature phase diagrams obtained from the electrical-resistivity data. At  $p = 3.1$  GPa, signatures of both the tetragonal high-temperature phase delimited by  $T_x = 235$  K and  $\mu_0 H_{x2}^{\text{up}} = 38$  T and the orthorhombic antiferromagnetic order established at temperatures below  $T_N$  are observed. This indicates that the crystal may be inhomogeneous, with the presence of orthorhombic and tetragonal domains. The

transition at  $H_{x2}$  exhibits a strong hysteresis at  $T = 10$  K, which weakens with increasing temperature. At  $p = 4.9$  GPa, the absence of the orthorhombic AF phase allows us to see the hysteresis of the two transitions at  $H_{x1}$  and  $H_{x2}$  at low temperatures. The temperature evolution of these two transitions is similar, their hystereses end at  $T \simeq 120$  K and their signatures disappear at temperatures above  $T_x$ . A temperature correction was applied for the  $H_{x2}^{\text{down}}$  data shown at temperatures  $T < 20$  K in these phase diagrams (see Supplemental Material [57]). The data collected at  $p = 6$  GPa are very similar to the data collected at  $p = 4.9$  GPa, but superconductivity with  $\rho = 0$  is only observed at  $p = 6$  GPa (in data collected at zero field or from low-field pulses, with a small electrical current, see next paragraph). No noticeable difference at the two pressures between the signatures of the transitions at the fields  $H_{x1}$  and  $H_{x2}$  is found. In Sec. IV D they will be identified as possible metamagnetic transitions.

Figure 9(a) presents the temperature dependence of the electrical resistivity of  $\text{UTe}_2$ , measured for different electrical currents, in zero field and at pressure  $p = 6$  GPa. With an electrical current  $I = 0.01$  mA, superconductivity with zero resistivity occurs below the temperature  $T_{\text{sc}} = 1.45$  K. For higher excitation currents, zero resistivity is not reached, but the onset of superconductivity can be defined at a temperature of  $\simeq 2.9$  K. A large temperature width, of  $\simeq 1.5$  K, of the superconducting transition is found. Smooth steplike anomalies in the electrical resistivity at temperatures between  $T_{\text{sc}}$  and 2.9 K indicate an inhomogeneous sample quality, possibly due to the nonhydrostatic pressure generated by our cell. Figure 9(b) shows the electrical resistivity measured with a current  $I = 0.2$  mA under a pressure  $p = 6$  GPa and magnetic fields up to  $\mu_0 H = 3$  T. This current was chosen to extract the superconducting phase boundary under the magnetic field with a good signal-over-noise ratio. However, it is much larger than the current of 0.01 mA at which zero resistivity was extracted below  $T_{\text{sc}}$ . This makes the characterization of  $H_{c2}$  defined with  $\rho = 0$  not possible and only the magnetic field at the onset of superconductivity can be extracted. We note that superconductivity could not be evidenced from the high-field-pulse data presented in Figs. 7(b) and 7(c) due to the large current  $I = 4$  mA used but also to the difficulty to extract the field variation of  $\rho$  at the very beginning of the pulses. The magnetic-field-temperature phase diagram in Fig. 9(c) shows the boundaries of the superconducting phase stabilized at  $p = 6$  GPa in a magnetic field applied along the direction  $\mathbf{c}'$  of the tetragonal structure (see Sec. IV B). This phase diagram is similar to that reported in [52] for a magnetic field applied along the direction  $\mathbf{c}$  of the orthorhombic structure, which can be identified as a direction titled in the  $(\mathbf{a}', \mathbf{c}')$  plane of the tetragonal structure (see Sec. IV B).

#### IV. DISCUSSION

The present work, in which  $\text{UTe}_2$  was investigated under pressures up to 6 GPa combined with magnetic fields tilted by  $30^\circ$  from  $\mathbf{b}$  towards  $\mathbf{c}$ , completes a former study of  $\text{UTe}_2$  under pressures up to 4 GPa combined with magnetic fields  $\mathbf{H} \simeq \parallel \mathbf{b}$  but with a  $15^\circ - 30^\circ$  misorientation of the sample [46,47]. Interestingly, similar pressure variations of the critical field  $H_m$  and of the Fermi-liquid coefficient  $A$  have been found in

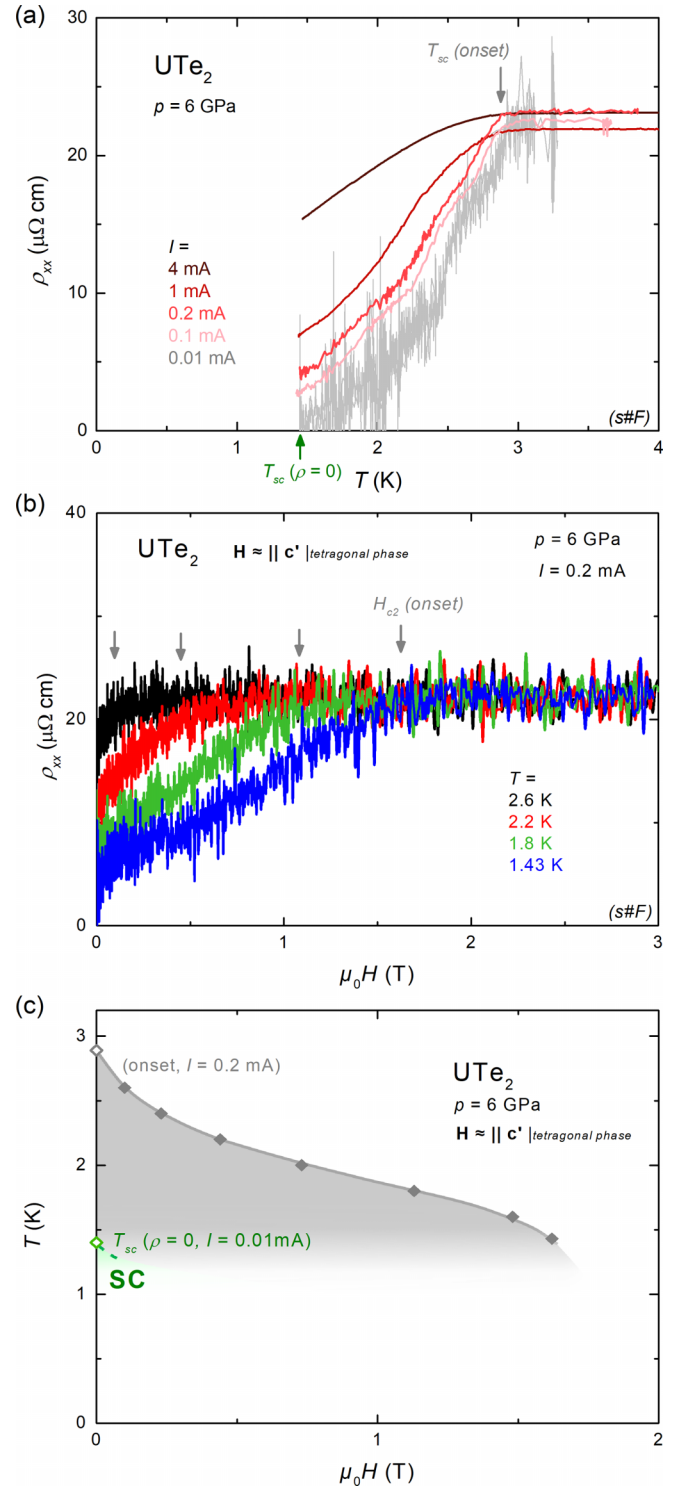


FIG. 9. (a) Temperature dependence of the electrical resistivity  $\rho_{xx}$  of  $\text{UTe}_2$  at  $p = 6$  GPa and zero magnetic field, measured with different electrical currents  $I$  varying from 0.01 mA to 4 mA. (b) Magnetic-field dependence of the electrical resistivity  $\rho_{xx}$  measured with a current  $I = 0.2$  mA, at temperatures from 1.43 K to 2.6 K and at  $p = 6$  GPa. (c) Magnetic-field-temperature phase diagram of the superconducting phase at  $p = 6$  GPa.

the two studies, and we suspect now that the field direction in [46,47] was probably near to that applied here (see discussion in the Supplemental Material [57]). While the two sets of data

are quite similar in the low-pressure orthorhombic phase, new information is collected here concerning the high-pressure tetragonal phase. Stronger field-induced anomalies are observed at the lowest temperature ( $T = 1.4$  K), presumably due to an increase of the sample quality (the sample studied here was grown by the molten-salt-flux method [58], while the samples studied in [46,47] were grown by the chemical-vapor-transport method [8]). A high-pressure and purely tetragonal phase with signatures of superconductivity is evidenced, and two field-induced transitions (instead of one in [46,47]) are found. A phase transition at  $T_x = 235$  K under high pressure was evidenced for the first time in our previous work [46,47]. It was later confirmed in [52], where it was identified as a signature of a high-pressure tetragonal phase beyond  $p^* = 3\text{--}8$  GPa (see also [53,54]). Concerning the low-pressure orthorhombic phase, incommensurate antiferromagnetism was recently evidenced under pressure beyond  $p_c = 1.7$  GPa [44]. In the light of these recent findings, we discuss below our new experimental data: the high-field properties of  $\text{UTe}_2$  in its orthorhombic phase are considered in Sec. IV A and the high-field properties of  $\text{UTe}_2$  in its tetragonal phase are considered in Secs. IV B, IV C, and IV D.

#### A. Magnetic and superconducting properties in the orthorhombic phase

Our study of  $\text{UTe}_2$  in a magnetic field tilted by  $30^\circ$  from  $\mathbf{b}$  towards  $\mathbf{c}$  confirms that the metamagnetic field  $H_m$  collapses in the vicinity of the critical pressure  $p_c$ , which was first reported in [48] (and in [46] but with a sample misorientation). In addition, we find here that the Fermi-liquid coefficient  $A$  is maximum at  $H_m$  and that its maximal value is enhanced near  $p_c$ , where  $H_m$  collapses. Knowing that the coefficient  $A$  is presumably driven by the magnetic fluctuations in the system, its variation in the  $(p, H)$  plane indicates the presence of stronger magnetic fluctuations at  $H_m$  and near  $p_c$ . The magnetic fluctuations have been proposed to play a crucial role for the development of superconductivity in  $\text{UTe}_2$ , as in other heavy-fermion compounds. Their enhancement near  $p_c$  may be responsible for the development of the pressure-induced superconducting phase SC2, while their enhancement near  $H_m$  may be responsible for the development of the field-induced superconducting phases SC2 (suspected, but not definitively proved, to be the same phase as that induced under pressure [40,38]) and SC-PPM near  $H_m$  [10,12]. In Ref. [48], a study combining temperatures down to 400 mK, steady fields up to 45 T and pressures up to 1.54 GPa permitted an extension of the phase SC-PPM to be revealed under pressure, with critical superconducting temperatures of less than 1 K. Due to the temperatures  $T \geq 1.4$  K investigated here, and perhaps to a nonoptimum tilting of the field direction, we could not observe the superconducting phase SC-PPM in our experimental data. At temperatures below  $T_N = 3.7$  K, we could observe the signature of a moment reorientation inside the antiferromagnetic phase. At  $p = 2.4$  GPa and  $T = 1.4$  K, a moment reorientation occurs at  $\mu_0 H_r = 2.5$  T and antiferromagnetism is destroyed beyond  $\mu_0 H_c = 13.5$  T. The variations of  $\rho_{xx}$  at  $H_r$  and  $H_c$  resemble those observed at  $H_{sf}$  and  $H_c$  in the prototypical Heisenberg antiferromagnet  $\text{YbNiSi}_3$  [61]. In  $\text{YbNiSi}_3$ , as in other weakly anisotropic

antiferromagnets, a spin-flop transition is induced at a magnetic  $H_{sf}$  applied parallel to the antiferromagnetic-moment directions [62]. In  $\text{UTe}_2$ , the magnetic anisotropy is strongly reduced at the critical pressure, as indicated by magnetic-susceptibility measurements [41], but moment reorientation processes have also been observed under a magnetic field applied along  $\mathbf{c}$ . Neutron diffraction experiments have also shown that the antiferromagnetic order induced under pressure is associated with an incommensurate propagation vector  $\mathbf{k}_m = (0.07, 0.67, 0)$  [44]. A component  $\mu_m^\perp = 0.3 \mu_b/U$  of the antiferromagnetic moments perpendicular to  $\mathbf{b}$  was extracted, indicating that the full antiferromagnetic moments have an amplitude  $\mu_m \geq 0.3 \mu_b/U$ , but the magnetic structure could not be resolved. Assuming a complex magnetic structure (for instance, a helical incommensurate structure in which the moment direction would rotate elliptically in space), subtle effects could be induced in a magnetic field (for instance, a selection of  $\mathbf{k}$  domains or a field-induced change of magnetic wave vector  $\mathbf{k}$ ; see  $\text{CeRhIn}_5$  [63]). In the future, efforts are needed to elucidate the antiferromagnetic structure of  $\text{UTe}_2$  and its modifications by a magnetic field, such as that observed indirectly at  $H_r$  by electrical resistivity here.

#### B. Field direction in the tetragonal phase

Honda *et al.* proposed three scenarios to describe the structural transition of  $\text{UTe}_2$  under pressure [52]. In each scenario a given group of atoms in the orthorhombic structure was identified as leading to an elementary cell of the tetragonal structure (see Supplemental Fig. S13 in the Supplemental Material [57]). One of the three scenarios, the first one proposed by Honda *et al.*, seems more likely than the two others. This scenario implies the smallest translations of the atoms and the smallest tilts of the atomic bonds at the structural transition, which contrasts with the more complex sets of atomic rearrangements needed for the second and third scenarios. In the following, we describe the structural transition with a given set of atomic displacements compatible with the first scenario. This allows us to determine the direction of the magnetic field applied here relative to the high-pressure tetragonal-phase main directions (see next paragraph), but also to discuss how a uniaxial pressure may affect the structural transition (see Sec. IV C).

Figure 10 presents three-dimensional views and projections along the  $(\mathbf{b}, \mathbf{c})$  plane (directions defined in the orthorhombic structure) of  $\text{UTe}_2$  atoms in their orthorhombic phase at  $p = 1$  bar [Insets (a,b)] and in their tetragonal phase at  $p > 3\text{--}8$  GPa [Insets (c,d)]. The low-pressure orthorhombic structure ( $Immm$ ) was drawn assuming the lattice parameters  $a = 4.16$  Å,  $b = 6.12$  Å, and  $c = 13.96$  Å, and the parameter  $z = 0.13544$  (position of the U atom in the cell) obtained at  $p = 1$  bar and  $T = 300$  K [3], and the high-pressure tetragonal structure ( $I4/mmm$ ) was drawn assuming the lattice parameters  $a' = 3.89$  Å and  $c' = 9.80$  Å obtained at  $p = 4$  GPa and  $T = 300$  K [52] (see unit cells of the two structures in Fig. 1). U atoms with magenta color and Te atoms with blue color form a unit cell in the high-pressure tetragonal phase and are also identified in the low-pressure orthorhombic phase, i.e., prior to the structural transition. In the Supplemental Material [57], we detail how the structural

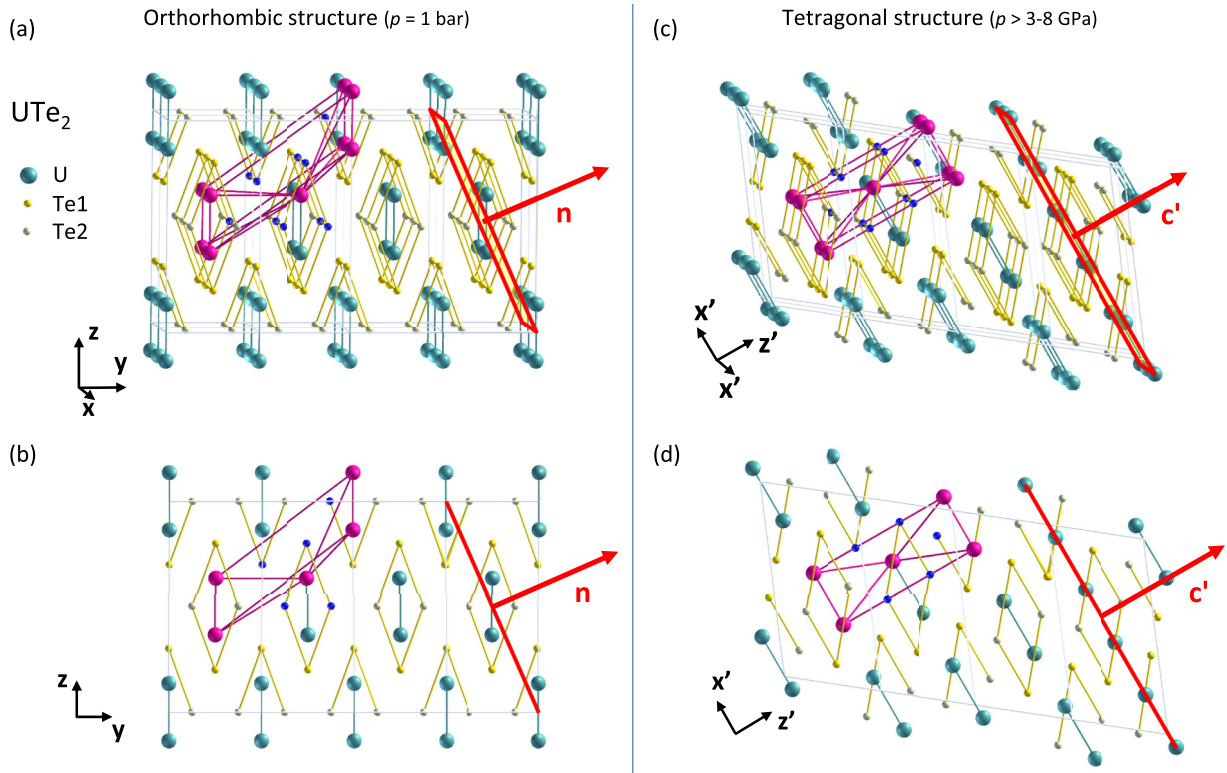


FIG. 10. Views of  $\text{UTe}_2$  in its low-pressure orthorhombic structure (a) in three dimensions and (b) projected along the plane  $\perp \mathbf{a}$ . Views of  $\text{UTe}_2$  in its high-pressure tetragonal structure (c) in three dimensions and (d) projected along the plane  $\perp \mathbf{a}$ . In (a), (b) the two-leg, U-atom ladders and their nearest Te-atom neighbors, and the plane perpendicular to  $\mathbf{n}$ , of Miller indices (0,1,1) are emphasized by different sets of colors. The same colors are kept in (c), (d) to visualize the effect of the pressure-induced structural transition on the atoms. U atoms with magenta color and Te atoms with blue color form a unit cell in the tetragonal structure.

transition can be artificially decomposed into five elementary steps corresponding to a given set of atomic displacements or lattice distortions. As shown in Fig. 10, the planes of Miller indices (0 1 1) and normal to the direction  $\mathbf{n}$  in the low-pressure orthorhombic structure [12] are transformed into the basal planes  $\perp \mathbf{c}'$  in the high-pressure tetragonal structure. In the present study, the magnetic field  $\mathbf{H}$  was applied in a direction tilted by  $30^\circ$  from  $\mathbf{b}$  towards  $\mathbf{c}$  in the low-pressure orthorhombic phase. This direction is very close to the direction  $\mathbf{n}$ , which is tilted by  $23.7^\circ$  from  $\mathbf{b}$  towards  $\mathbf{c}$ , indicating that  $\mathbf{H}$  was applied near to the direction  $\mathbf{c}'$  in the high-pressure tetragonal phase.

In addition to their role for the structural transition, the planes of Miller indices (0 1 1) are an important feature of the orthorhombic structure. It was noticed that they are cleaving planes of the crystal, and a possible relation with the stabilization of the field-induced superconducting phase SC-PPM in a magnetic field  $\mathbf{H} \simeq \parallel \mathbf{n}$  was emphasized [12]. It is also clear from Figs. 10(a) and 10(b) that in the low-pressure orthorhombic phase, Te atoms are already almost lying within planes  $\perp \mathbf{n}$ . Assuming a larger electronegativity of Te atoms in comparison with that of U atoms, these Te planes may constitute negative-charge reservoirs. A question is whether they could play a role for the stabilization of the different superconducting phases of  $\text{UTe}_2$  in its orthorhombic structure, for instance, the phase SC-PPM induced in magnetic fields  $\mathbf{H} \simeq \parallel \mathbf{n}$  beyond  $H_m$ . Another question is how the valence change observed at the structural transition [55,54], which

could be related with a modification of the charges on Te and U atoms, may be involved in the drastic change of the magnetic and superconducting properties in the tetragonal phase.

### C. Effects of a uniaxial pressure

Different critical pressures  $p^*$ , ranging from 3 to 8 GPa, of the structural transition were determined from the study of powdered samples and single crystals of  $\text{UTe}_2$  (see here and in Refs. [46,47,53,52]). In Ref. [53] (x-ray diffraction) nonhydrostatic conditions of pressure on powdered samples were identified as driving to the increase of  $p^*$ , from 5 GPa under hydrostatic pressure up to 8 GPa under nonhydrostatic pressure. In [52] (x-ray diffraction and electrical resistivity) a smaller critical pressure  $p^* \simeq 3.5\text{--}4$  GPa was found for single crystals of main faces with Miller indices (1 0 0) and (1 1 0). In the same work, a critical pressure  $p^* \simeq 5$  GPa was determined for powder crystals, for which the orthorhombic and tetragonal domains were found to coexist under pressures from 5 to 7 GPa. In the studies presented here and in [46,47] (electrical resistivity), signatures of the tetragonal phase were observed under pressures  $p > 3.1$  GPa, indicating a critical pressure  $p^* \lesssim 3$  GPa, for  $\mathbf{H}$  tilted by  $\simeq 25^\circ\text{--}30^\circ$  from  $\mathbf{b}$  to  $\mathbf{c}$  (see Supplemental Material [57]). Oppositely, the signatures of the high-pressure tetragonal phase were not observed under pressures  $p \leq 4$  GPa, indicating a critical pressure  $p^* \gtrsim 4$  GPa, for  $\mathbf{H}$  applied along  $\mathbf{c}$  [46,47].

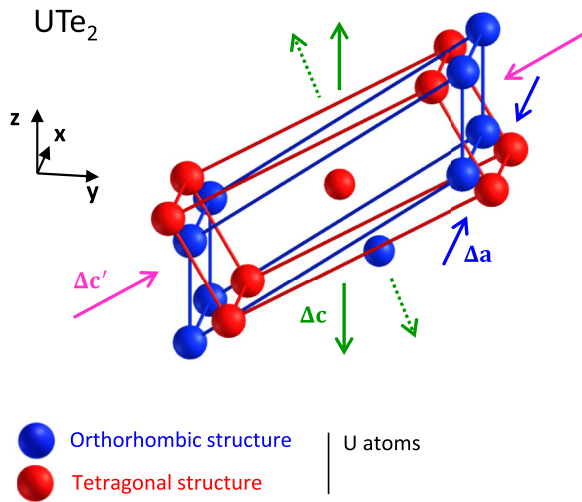


FIG. 11. Comparison of the positions of a group of atoms forming a unit cell in the high-pressure tetragonal structure and their positions in the low-pressure orthorhombic structure, emphasizing the lattice distortions (indicated schematically by arrows) induced at the structural transition.

Here we attempt to discuss the effects on single crystals from a nonhydrostatic pressure in the cells used here and in [46,47]. As shown schematically in Fig. 11, the stabilization of the high-pressure tetragonal phase is associated with a contraction of the lattice along the direction  $\mathbf{c}'$  of the tetragonal structure (or almost equivalently along the direction  $\mathbf{n}$  of the orthorhombic structure) and with an expansion along directions  $\mathbf{a}$  and  $\mathbf{c}$  of the orthorhombic structure. Uniaxial pressures applied parallel or perpendicularly to a direction close to  $\mathbf{n}$  may therefore favor or unfavor, respectively, the establishment of a tetragonal phase in comparison the effect of a purely hydrostatic pressure [52–54]. The pressure cell used here and in [46,47] was set up with its vertical axis parallel to the magnetic field, indicating that uniaxial pressures may have been generated along a direction parallel to the field. This may explain why the signatures of the structural transition were observed above moderate pressures of  $\simeq 3$  GPa in a field tilted by  $\simeq 30^\circ$  from  $\mathbf{b}$  towards  $\mathbf{c}$  in Refs. [46,47] and in this work but were not observed in fields  $\mathbf{H} \parallel \mathbf{c}$  under pressures up to 4 GPa in Refs. [46,47]. We note that, in the present work, the field  $H_{x2}$  is found to be almost independent of pressure in the pressure range 4.9–6 GPa. The transition at  $H_{x2}$  may therefore also be almost insensitive to uniaxial pressure components in this high-pressure range. Thus the sharpness of the transition at  $H_{x2}^{\text{up}}$  [see Fig. 7(a)] cannot be considered as an indication for a uniform uniaxial pressure component within the cell chamber where the sample is.

In addition to effects induced by nonhydrostatic conditions of pressure, the critical pressure and its hysteresis are also expected to depend on the temperature and sample quality. The value of the critical pressure  $p^*$  at the structural transition was found to increase at low temperature, varying from 3.5 to 4 GPa at room temperature to 5.5 GPa at  $T = 29$  K, from a study using a cell offering very good hydrostatic conditions in [52]. However, detailed temperature-dependent measurements of the structure were not presented in [52]. Different values

of  $p^*$  are therefore expected, depending on if the pressure was changed at low temperature (as in [35,52]) or at room temperature (as here and in [46,53,54]). Knowing that the structural transition is associated with a large hysteresis, the chronology of the pressure and temperature tunings therefore has to be considered carefully. For samples of lower quality, i.e., with a high number of defects, a larger hysteresis and thus a larger critical pressure  $p^*$  when the pressure is increased, possibly accompanied by a broadening of the transition, may also be expected.

#### D. Magnetic order in the tetragonal phase?

Different elements support that magnetic order may be stabilized below the transition temperature  $T_x$  in the tetragonal phase of  $\text{UTe}_2$  (see also discussion in [52]). The electrical resistivity presents a similar variation at  $T_x$  than that observed at the transition temperature of other uranium compounds where high-temperature magnetic order was evidenced. Examples are the ferromagnets  $\text{UTe}$ ,  $\text{USE}$ , and  $\text{US}$  associated with the Curie temperatures  $T_C \simeq 100$  K, 160 K, and 177 K, respectively [64], and the antiferromagnets  $\text{USb}_2$  and  $\text{UAs}_2$  associated with Néel temperatures  $T_N = 202$  K and 270 K, respectively [65,66]. Steplike variations of the low-temperature electrical resistivity of  $\text{UTe}_2$  were also observed at the magnetic fields  $H_{x1}$  and  $H_{x2}$ . They transform into kinks in the electrical resistivity at temperatures  $T \lesssim T_x = 235$  K and disappear at temperatures larger than  $T_x$ . The transitions at  $H_{x1}$  and  $H_{x2}$  are therefore a property of the electronic state stabilized below the transition temperature  $T_x$ . Assuming that  $T_x$  is the temperature of a magnetic phase transition, we identify the anomalies at  $H_{x1}$  and  $H_{x2}$  as the signatures of possible metamagnetic transitions, i.e., first-order transitions associated with a sudden increase of the magnetization induced by a reorientation of the magnetic moments. In the case of a ferromagnet with a strong magnetic anisotropy, metamagnetism can be induced by a magnetic field applied perpendicular to the ferromagnetic moments, as observed, for instance, in  $\text{URhGe}$  [67]. However, metamagnetism is generally observed in antiferromagnets, either with a small magnetic anisotropy (“spin-flop” transition) or with a strong magnetic anisotropy, when the magnetic field is applied parallel to the antiferromagnetic moments direction [62]. Steplike variations in the magnetization and magnetostriction were, for instance, observed in the antiferromagnet  $\text{USb}_2$  at temperatures smaller than  $T_N$ , indicating a first-order metamagnetic transition [68]. In  $\text{UTe}_2$ , antiferromagnetic moments may be fully aligned, or partly tilted, along or near the direction  $\mathbf{c}'$  of the tetragonal structure. Magnetization measurements showing steplike increases of the magnetization at  $H_{x1}$  and  $H_{x2}$  are needed to confirm that these transitions are metamagnetic. Alternatively, we cannot exclude that the transitions at  $T_x$  and  $H_x$  may be driven by a valence transition, as observed, for instance, in  $\text{YbInCu}_4$  [69]. We also note that the two transitions fields  $H_{x1}$  and  $H_{x2}$  observed here, which share a similar temperature evolution up to  $T_x$ , may be induced by two crystalline domains formed under pressure and aligned differently relative to the magnetic field. A single transition field  $H_x$  was observed in the study made in [46,47], suggesting then a dominant domain.

The possibility of crystalline domains in the present study may be related with the observation by x-ray diffraction of two domains in the high-pressure tetragonal phase [52]. In the future, challenges will be to characterize the nature of the electronic state, possibly of magnetic origin as suspected here, which is established below the transition temperature  $T_x$ , and to study if the formation of domains may be related with the doubling of the metamagnetic transition or if multiple metamagnetic transitions could be an intrinsic high-field property of the system.

## ACKNOWLEDGMENTS

We acknowledge useful discussion with Fuminori Honda and financial support from the French National Research Agency through the collaborative research project FRESCO No. ANR-20-CE30-0020, from the Cross-Disciplinary Program on Instrumentation and Detection of CEA, the French Alternative Energies and Atomic Energy Commission, and from the JSPS KAKENHI Grants No. JP19H00646, No. 19K03756, No. JP20H00130, No. 20H01864, No. JP20K20889, No. JP20KK0061, and No. 21H04987.

- 
- [1] D. Aoki, J.-P. Brison, J. Flouquet, K. Ishida, G. Knebel, Y. Tokunaga, and Y. Yanase, *J. Phys.: Condens. Matter* **34**, 243002 (2022).
- [2] S. K. Lewin, C. E. Frank, S. Ran, J. Paglione, and N. P. Butch, *Rep. Prog. Phys.* **86**, 114501 (2023).
- [3] S. Ikeda, H. Sakai, D. Aoki, Y. Homma, E. Yamamoto, A. Nakamura, Y. Shiokawa, Y. Haga, and Y. Ōnuki, *J. Phys. Soc. Jpn.* **75**, 116 (2006).
- [4] A. Miyake, Y. Shimizu, Y. J. Sato, D. Li, A. Nakamura, Y. Homma, F. Honda, J. Flouquet, M. Tokunaga, and D. Aoki, *J. Phys. Soc. Jpn.* **88**, 063706 (2019).
- [5] Y. S. Eo, S. Liu, S. R. Saha, H. Kim, S. Ran, J. A. Horn, H. Hodovanets, J. Collini, T. Metz, W. T. Fuhrman, A. H. Nevidomskyy, J. D. Denlinger, N. P. Butch, M. S. Fuhrer, L. A. Wray, and J. Paglione, *Phys. Rev. B* **106**, L060505 (2022).
- [6] S. Ran, C. Eckberg, Q.-P. Ding, Y. Furukawa, T. Metz, S. R. Saha, I.-L. Liu, M. Zic, H. Kim, J. Paglione, and N. P. Butch, *Science* **365**, 684 (2019).
- [7] C. Paulsen, G. Knebel, G. Lapertot, D. Braithwaite, A. Pourret, D. Aoki, F. Hardy, J. Flouquet, and J.-P. Brison, *Phys. Rev. B* **103**, L180501 (2021).
- [8] D. Aoki, A. Nakamura, F. Honda, D. Li, Y. Homma, Y. Shimizu, Y. J. Sato, G. Knebel, J.-P. Brison, and A. Pourret, *J. Phys. Soc. Jpn.* **88**, 043702 (2019).
- [9] G. Knebel, W. Knafo, A. Pourret, Q. Niu, M. Vališka, D. Braithwaite, G. Lapertot, M. Nardone, A. Zitouni, S. Mishra, I. Sheikin, G. Seyfarth, J.-P. Brison, D. Aoki, and J. Flouquet, *J. Phys. Soc. Jpn.* **88**, 063707 (2019).
- [10] S. Ran, I.-L. Liu, Y. S. Eo, D. J. Campbell, P. Neves, W. T. Fuhrman, S. R. Saha, C. Eckberg, H. Kim, J. Paglione, D. Graf, J. Singleton, and N. P. Butch, *Nat. Phys.* **15**, 1250 (2019).
- [11] A. Rosuel, C. Marcenat, G. Knebel, T. Klein, A. Pourret, N. Marquardt, Q. Niu, S. Rousseau, A. Demuer, G. Seyfarth, G. Lapertot, D. Aoki, D. Braithwaite, J. Flouquet, and J.-P. Brison, *Phys. Rev. X* **13**, 011022 (2023).
- [12] W. Knafo, M. Nardone, M. Vališka, A. Zitouni, G. Lapertot, D. Aoki, G. Knebel, and D. Braithwaite, *Commun. Phys.* **4**, 40 (2021).
- [13] R. Schönemann, P. F. Rosa, S. M. Thomas, Y. Lai, D. N. Nguyen, J. Singleton, E. L. Brosha, R. D. McDonald, V. Zapf, B. Maiorov, and M. Jaime, *PNAS Nexus* **3**, 1 (2024).
- [14] T. Helm, M. Kimata, K. Sudo, A. Miyata, J. Stirnat, T. Förster, J. Hornung, M. König, I. Sheikin, A. Pourret, G. Lapertot, D. Aoki, G. Knebel, J. Wosnitza, and J.-P. Brison, *Nat. Commun.* **15**, 37 (2024).
- [15] A. Miyake, Y. Shimizu, Y. J. Sato, D. Li, A. Nakamura, Y. Homma, F. Honda, J. Flouquet, M. Tokunaga, and D. Aoki, *J. Phys. Soc. Jpn.* **90**, 103702 (2021).
- [16] W. Knafo, M. Vališka, D. Braithwaite, G. Lapertot, G. Knebel, A. Pourret, J.-P. Brison, J. Flouquet, and D. Aoki, *J. Phys. Soc. Jpn.* **88**, 063705 (2019).
- [17] S. K. Lewin, P. Czajka, C. E. Frank, G. S. Salas, H. Yoon, Y. S. Eo, J. Paglione, A. H. Nevidomskyy, J. Singleton, and N. P. Butch, [arXiv:2402.18564](https://arxiv.org/abs/2402.18564).
- [18] Z. Wu, T. Weinberger, A. J. Hickey, D. V. Chichinadze, D. Shaffer, A. Cabala, H. Chen, M. Long, T. Brumm, W. Xie, Y. Lin, Y. Skourski, Z. Zengwei, D. Graf, V. Sechovsky, G. Lonzarich, M. Vališka, F. Grosche, and A. Eaton, [arXiv:2403.02535](https://arxiv.org/abs/2403.02535).
- [19] C. Duan, K. Sasmal, M. B. Maple, A. Podlesnyak, J.-X. Zhu, Q. Si, and P. Dai, *Phys. Rev. Lett.* **125**, 237003 (2020).
- [20] W. Knafo, G. Knebel, P. Steffens, K. Kaneko, A. Rosuel, J.-P. Brison, J. Flouquet, D. Aoki, G. Lapertot, and S. Raymond, *Phys. Rev. B* **104**, L100409 (2021).
- [21] N. P. Butch, S. Ran, S. R. Saha, P. M. Neves, M. P. Zic, J. Paglione, S. Gladchenko, Q. Ye, and J. A. Rodriguez-Rivera, *npj Quantum Mater.* **7**, 39 (2022).
- [22] Y. Tokunaga, H. Sakai, S. Kambe, T. Hattori, N. Higa, G. Nakamine, S. Kitagawa, K. Ishida, A. Nakamura, Y. Shimizu, Y. Homma, D. Li, F. Honda, and D. Aoki, *J. Phys. Soc. Jpn.* **88**, 073701 (2019).
- [23] Y. Tokunaga, H. Sakai, S. Kambe, Y. Haga, Y. Tokiwa, P. Opletal, H. Fujibayashi, K. Kinjo, S. Kitagawa, K. Ishida, A. Nakamura, Y. Shimizu, Y. Homma, D. Li, F. Honda, and D. Aoki, *J. Phys. Soc. Jpn.* **91**, 023707 (2022).
- [24] C. Duan, R. Baumbach, A. Podlesnyak, Y. Deng, C. Moir, A. J. Breindel, M. B. Maple, E. Nica, Q. Si, and P. Dai, *Nature (London)* **600**, 636 (2021).
- [25] S. Raymond, W. Knafo, G. Knebel, K. Kaneko, J.-P. Brison, J. Flouquet, D. Aoki, and G. Lapertot, *J. Phys. Soc. Jpn.* **90**, 113706 (2021).
- [26] P. Monthoux, D. Pines, and G. Lonzarich, *Nature (London)* **450**, 1177 (2007).
- [27] Y. Tokunaga, H. Sakai, S. Kambe, P. Opletal, Y. Tokiwa, Y. Haga, S. Kitagawa, K. Ishida, D. Aoki, G. Knebel, G. Lapertot, S. Krämer, and M. Horvatić, *Phys. Rev. Lett.* **131**, 226503 (2023).
- [28] T. Thebault, M. Vališka, G. Lapertot, A. Pourret, D. Aoki, G. Knebel, D. Braithwaite, and W. Knafo, *Phys. Rev. B* **106**, 144406 (2022).
- [29] J. Ishizuka and Y. Yanase, *Phys. Rev. B* **103**, 094504 (2021).

- [30] A. Kreisel, Y. Quan, and P. J. Hirschfeld, *Phys. Rev. B* **105**, 104507 (2022).
- [31] T. Shishidou, H. G. Suh, P. M. R. Brydon, M. Weinert, and D. F. Agterberg, *Phys. Rev. B* **103**, 104504 (2021).
- [32] J. Tei, T. Mizushima, and S. Fujimoto, *Phys. Rev. B* **109**, 064516 (2024).
- [33] G. Nakamine, S. Kitagawa, K. Ishida, Y. Tokunaga, H. Sakai, S. Kambe, A. Nakamura, Y. Shimizu, Y. Homma, D. Li, F. Honda, and D. Aoki, *J. Phys. Soc. Jpn.* **88**, 113703 (2019).
- [34] G. Nakamine, K. Kinjo, S. Kitagawa, K. Ishida, Y. Tokunaga, H. Sakai, S. Kambe, A. Nakamura, Y. Shimizu, Y. Homma, D. Li, F. Honda, and D. Aoki, *J. Phys. Soc. Jpn.* **90**, 064709 (2021).
- [35] D. Braithwaite, M. Vališka, G. Knebel, G. Lapertot, J.-P. Brison, A. Pourret, M. Zhitomirsky, J. Flouquet, F. Honda, and D. Aoki, *Commun. Phys.* **2**, 147 (2019).
- [36] D. Aoki, F. Honda, G. Knebel, D. Braithwaite, A. Nakamura, D. Li, Y. Homma, Y. Shimizu, Y. J. Sato, J.-P. Brison, and J. Flouquet, *J. Phys. Soc. Jpn.* **89**, 053705 (2020).
- [37] S. Thomas, F. Santos, M. Christensen, T. Asaba, F. Ronning, J. Thompson, E. Bauer, R. Fernandes, G. Fabbris, and P. Rosa, *Sci. Adv.* **6**, eabc8709 (2020).
- [38] K. Kinjo, H. Fujibayashi, H. Matsumura, F. Hori, S. Kitagawa, K. Ishida, Y. Tokunaga, H. Sakai, S. Kambe, A. Nakamura, Y. Shimizu, Y. Homma, D. Li, F. Honda, and D. Aoki, *Sci. Adv.* **9**, eadg2736 (2023).
- [39] Z. Wu, J. Chen, T. Weinberger, A. Cabala, V. Sechovsky, M. Vališka, P. L. Alireza, A. Eaton, and F. Grosche, [arXiv:2403.06650](https://arxiv.org/abs/2403.06650).
- [40] W.-C. Lin, D. J. Campbell, S. Ran, I.-L. Liu, H. Kim, A. H. Nevidomskyy, D. Graf, N. P. Butch, and J. Paglione, *npj Quantum Mater.* **5**, 68 (2020).
- [41] D. Li, A. Nakamura, F. Honda, Y. J. Sato, Y. Homma, Y. Shimizu, J. Ishizuka, Y. Yanase, G. Knebel, J. Flouquet, and D. Aoki, *J. Phys. Soc. Jpn.* **90**, 073703 (2021).
- [42] K. Kinjo, H. Fujibayashi, G. Nakamine, S. Kitagawa, K. Ishida, Y. Tokunaga, H. Sakai, S. Kambe, A. Nakamura, Y. Shimizu, Y. Homma, D. Li, F. Honda, and D. Aoki, *Phys. Rev. B* **105**, L140502 (2022).
- [43] D. V. Ambika, Q.-P. Ding, K. Rana, C. E. Frank, E. L. Green, S. Ran, N. P. Butch, and Y. Furukawa, *Phys. Rev. B* **105**, L220403 (2022).
- [44] W. Knafo, T. Thebault, P. Manuel, D. D. Khalyavin, F. Orlandi, E. Ressouche, K. Beauvois, G. Lapertot, K. Kaneko, D. Aoki, D. Braithwaite, G. Knebel, and S. Raymond, [arXiv:2311.05455](https://arxiv.org/abs/2311.05455).
- [45] G. Knebel, M. Kimata, M. Vališka, F. Honda, D. Li, D. Braithwaite, G. Lapertot, W. Knafo, A. Pourret, Y. J. Sato, Y. Shimizu, T. Kihara, J.-P. Brison, J. Flouquet, and D. Aoki, *J. Phys. Soc. Jpn.* **89**, 053707 (2020).
- [46] M. Vališka, W. Knafo, G. Knebel, G. Lapertot, D. Aoki, and D. Braithwaite, *Phys. Rev. B* **104**, 214507 (2021).
- [47] See the Supplemental Material associated with [46].
- [48] S. Ran, S. R. Saha, I.-L. Liu, D. Graf, J. Paglione, and N. P. Butch, *npj Quantum Mater.* **6**, 75 (2021).
- [49] D. Aoki, M. Kimata, Y. J. Sato, G. Knebel, F. Honda, A. Nakamura, D. Li, Y. Homma, Y. Shimizu, W. Knafo, D. Braithwaite, M. Vališka, A. Pourret, J.-P. Brison, and J. Flouquet, *J. Phys. Soc. Jpn.* **90**, 074705 (2021).
- [50] H. Kim, I.-L. Liu, W.-C. Lin, Y. S. Eo, S. Ran, N. P. Butch, and J. Paglione, [arXiv:2307.00180](https://arxiv.org/abs/2307.00180).
- [51] G. Knebel, A. Pourret, S. Rousseau, N. Marquardt, D. Braithwaite, F. Honda, D. Aoki, G. Lapertot, W. Knafo, G. Seyfarth, J.-P. Brison, and J. Flouquet, *Phys. Rev. B* **109**, 155103 (2024).
- [52] F. Honda, S. Kobayashi, N. Kawamura, S. I. Kawaguchi, T. Koizumi, Y. J. Sato, Y. Homma, N. Ishimatsu, J. Gouchi, Y. Uwatoko, H. Harima, J. Flouquet, and D. Aoki, *J. Phys. Soc. Jpn.* **92**, 044702 (2023).
- [53] L. Q. Huston, D. Y. Popov, A. Weiland, M. M. Bordelon, P. F. S. Rosa, R. L. Rowland, B. L. Scott, G. Shen, C. Park, E. K. Moss, S. M. Thomas, J. D. Thompson, B. T. Sturtevant, and E. D. Bauer, *Phys. Rev. Mater.* **6**, 114801 (2022).
- [54] Y. Deng, E. Lee-Wong, C. M. Moir, R. S. Kumar, N. Swedan, C. Park, D. Y. Popov, Y. Xiao, P. Chow, R. E. Baumbach, R. J. Hemley, and M. B. Maple, [arXiv:2401.05586](https://arxiv.org/abs/2401.05586).
- [55] F. Wilhelm, J.-P. Sanchez, D. Braithwaite, G. Knebel, G. Lapertot, and A. Rogalev, *Commun. Phys.* **6**, 96 (2023).
- [56] K. Hu, Y. Zhao, Y. Geng, J. Yu, and Y. Gu, *Phys. Lett. A* **451**, 128401 (2022).
- [57] See Supplemental Material at <http://link.aps.org/supplemental/10.1103/PhysRevB.109.214420> for complementary graphs about raw data, details about the analysis made to extract the phase diagrams and the Fermi-liquid coefficient  $A$ , a discussion about atomic displacements at the pressure-induced structural transition, and a comparison of the results obtained here and those from a previous study published in [46,47].
- [58] H. Sakai, P. Opletal, Y. Tokiwa, E. Yamamoto, Y. Tokunaga, S. Kambe, and Y. Haga, *Phys. Rev. Mater.* **6**, 073401 (2022).
- [59] D. Braithwaite, W. Knafo, R. Settai, D. Aoki, S. Kurahashi, and J. Flouquet, *Rev. Sci. Instrum.* **87**, 023907 (2016).
- [60] R. Settai, W. Knafo, D. Braithwaite, S. Kurahashi, D. Aoki, and J. Flouquet, *Rev. High Pressure Sci. Technol.* **25**, 325 (2015).
- [61] K. Grube, T. Wolf, P. Adelmann, C. Meingast, and H. Löhneysen, *Phys. B: Condens. Matter* **378-380**, 750 (2006).
- [62] W. Knafo, [arXiv:2107.13458](https://arxiv.org/abs/2107.13458).
- [63] S. Raymond, E. Ressouche, G. Knebel, D. Aoki, and J. Flouquet, *J. Phys.: Condens. Matter* **19**, 242204 (2007).
- [64] J. Schoenes, *J. Less-Common Met.* **121**, 87 (1986).
- [65] P. Wiśniewski, D. Aoki, K. Miyake, N. Watanabe, Y. Inada, R. Settai, Y. Haga, E. Yamamoto, and Y. Ōnuki, *Phys. B: Condens. Matter* **281-282**, 769 (2000).
- [66] R. Wawryk, *Philos. Mag.* **86**, 1775 (2006).
- [67] F. Lévy, I. Sheikin, B. Grenier, and A. D. Huxley, *Science* **309**, 1343 (2005).
- [68] R. L. Stillwell, I.-L. Liu, N. Harrison, M. Jaime, J. R. Jeffries, and N. P. Butch, *Phys. Rev. B* **95**, 014414 (2017).
- [69] Y. H. Matsuda, T. Inami, K. Ohwada, Y. Murata, H. Nojiri, Y. Murakami, H. Ohta, W. Zhang, and K. Yoshimura, *J. Phys. Soc. Jpn.* **76**, 034702 (2007).